Pushing the limits of capillary assembly for the arbitrary positioning of sub-50nm nanocubes in printable plasmonic surfaces

Anna Capitaine, Muhammad Fajri, Beniamino Sciacca

To cite this version:

Anna Capitaine, Muhammad Fajri, Beniamino Sciacca. Pushing the limits of capillary assembly for the arbitrary positioning of sub-50nm nanocubes in printable plasmonic surfaces. Small Methods, 2023, 10.1002/smtd.202300373 . hal-04129724

HAL Id: hal-04129724
https://hal.science/hal-04129724v1

Submitted on 15 Jun 2023

Pushing the limits of capillary assembly for the arbitrary positioning of sub-50nm nanocubes in printable plasmonic surfaces

Anna Capitaine Muhammad L. Fajri Beniamino Sciacca*

Aix Marseille Univ, CNRS, CINaM, AMUtech, Marseille, France
*beniamino.sciacca@cnrs.fr

Keywords: *Capillary assembly, bottom-up, nanocube, epitaxy, welding, plasmonic metasurface*

The fabrication of high quality nanophotonic surfaces for integration in optoelectronic devices remains a challenge because of the complexity and cost of top-down nanofabrication strategies. Combining colloidal synthesis with templated self-assembly emerged as an appealing low-cost solution. However, it still faces several obstacles before integration in devices can become a reality. This is mostly due to the difficulty in assembling small nanoparticles (<50 nm) in complex nanopatterns with a high yield. In this study, we propose a reliable methodology to fabricate printable nanopatterns with an aspect ratio varying from 1 to 10 and a lateral resolution of 30 nm via nanocube assembly and epitaxy. Investigating templated assembly via capillary forces, we identified a new regime that we used to assemble 30 to 40 nm nanocubes in a patterned PDMS template with a high yield for both Au and Ag with multiple particles per trap. This new method relies on the generation and control of an accumulation zone at the contact line that is thin as opposed to dense, displaying higher versatility. This is in contrast with conventional wisdom, identifying a dense accumulation zone as a requirement for high-yield assembly. In addition, we propose different formulations that can be used for the colloidal dispersion, showing that the standard water-surfactant solutions can be replaced by surfactant-free ethanol solutions, with good assembly yield. This allows to minimize the presence of surfactants that could affect electronic properties. Finally, we show that the obtained nanocube arrays can be transformed into continuous monocrystalline nanopatterns via nanocube epitaxy at near ambient temperature, and transferred to different substrates via contact printing. This approach opens new doors to the templated assembly of small colloids and could find potential applications in various optoelectronic devices ranging from solar cells to light-emitting diodes and displays.

1 Introduction

Nanoparticles and nanostructures with sub-micron dimensions can interact strongly with light. In particular, plasmonic nanoparticles exhibit strong resonances, that depend on material composition, nanoparticle geometry (size and shape) and dielectric environment [1, 2, 3, 4, 5, 6, 7]. Additionally, their geometrical arrangement on a surface enables them to tailor how light is scattered, absorbed or propagates for specific applications. These include nanophotonics for photovoltaics [8], surface-enhanced spectroscopy [9, 10, 11, 12], catalysis [13, 14, 15], sensing [16, 17, 12], and in some example they have been integrated in portable devices [18] or built monolitically on complementary metal oxide semiconductor photodiodes [19] .

The realization of such metasurfaces is commonly achieved by top-down techniques. In particular, the combination of electron-beam lithography (EBL), evaporation and lift-off processes or etching steps can be used to achieve nanostructures of arbitrary shapes precisely positioned on a surface, with nanometric resolution. This allows to obtain complex nanophotonic surfaces as proof of concepts, but material quality is often poor and these approaches are time consuming, expensive and not scalable [20].

Alternatively, Nanoimprint Lithography (NIL) has emerged as a promising solution to build nanostructures over a large area while maintaining nanometric resolution. This is enabled by the replication of an EBL master to polydimethylsiloxane (PDMS), that can be used multiple times to pattern materials. Metals are, however, challenging to obtain via NIL because metallic precursors require the presence of organic additives (eventually removed by heat treatment), which substantially deteriorates material quality with a direct impact on their scattering and absorption cross-sections [21, 22, 23].

On the other hand, plasmonic nanoparticles obtained via colloidal synthesis are typically single crystals of the highest quality, which makes them ideal constituents to reach ultimate performance upon spatial arrangement on surfaces [24, 25].

Among the various tools available to induce their assembly, templated assembly via capillary forces is highly promising as it allows for the large-scale arrangement of particles into arbitrary configurations at low cost [26]. Using EBL to fabricate the templates combines the best of two worlds: nanoscale precision of top-down techniques and low-cost, scalability and material quality offered by bottom-up solution routes

[24]. Similarly to NIL, PDMS is used to create limitless replica of the EBL master, and assembly is performed by dragging an aqueous colloidal solution over the nanostructured PDMS template, to trap nanoparticles in the PDMS trenches. High-yield assembly is highly dependent on the formation of a dense particle accumulation zone (AZ) at the meniscus front line, driven by a convective flow arising from solvent evaporation [27], and on the direction of the capillary forces, which depends both on contact angle and meniscus pinning at trap edges (see next) [27].

Importantly, the low surface energy of PDMS makes it possible to swiftly integrate assembled nanoparticles into devices by contact printing if the assembly is performed in shallow traps [28]. Capillary assembly thus combines the advantages of high-quality materials, low-cost fabrication, and potential for large-area integration. However, the shape of nanostructures is often limited to that of Platonic solids that can be produced through colloidal synthesis, which hinders the creation of intricate nanophotonic surfaces composed of individual units with arbitrary geometries. This barrier can be lifted by employing single-crystalline nanocubes as building blocks that guarantee an identical crystallographic orientation of individual units when assembled face-to-face. Epitaxial welding of adjacent nanocubes assembled in the same traps enabled the formation of continuous monocrystalline structures in solution [29, 30]. In particular, it was demonstrated that gold nanocubes assembled in a PDMS template could be processed into a continuous material, making it possible to swiftly integrate such monocrystalline nanostructures into devices by contact printing [30].

The assembly of <100 nm nanoparticles is, however, challenging and constitutes an obstacle to the implementation of this technique for complex shapes and materials (see next). In particular, to the best of our knowledge, there are only two reports of capillary assembly of nanoparticles with all dimensions below 50 nm [31, 32]. In addition, <100 nm nanoparticles were in their vast majority assembled in trenches designed for single particle trapping, and all <60 nm nanoparticles were assembled in traps deeper than the particles size (**Table 1**).

Here we propose a framework for capillary assembly of <50 nm nanocubes (Ag, Au) that can be processed into printable monocrystalline nanophotonic surfaces upon nanocube epitaxy. The PDMS template is designed with traps that accommodate 30 to 40 nm nanocubes in a face-to-face configuration, organized into nanophotonic arrays. The nanopattern depth on the order of nanocube size allows to transfer the nanostructures by contact printing after assembly. We show that by finely monitoring AZ properties and contact angle, capillary assembly can be downscaled to nanocubes <50 nm with high yield, with multiple particles per trap assembled parallel to the contact line for the first time. furthermore, such nanostructure arrays exhibit sharp resonances when probed by spectroscopy and can be deposited on arbitrary substrates, opening the way to swift integration into devices as nanophotonic surfaces.

Next, we briefly discuss the impact of some parameters, such as pattern density and the nanocube surface chemistry, on the assembly yield. We highlight that the assembly of small nanoparticles is highly sensitive to defects, and the working conditions are narrow. We relate these observations to the strong van der Waals interactions among nanocubes in a dense crystalline AZ. This prompted us to explore the parameter space to identify new assembly regimes characterized by a smaller AZ, in which the interaction between nanocubes is mitigated. We show that such regimes can be either obtained by dilution, by increasing capping agent concentration or by using PVP-capped nanocubes in a mixture of ethanol and water as a solvent.

Finally, we show that these nanocube arrays could be transformed into continuous plasmonic nanostructures of various aspect ratios via nanocube epitaxy.

Substrate	**Material**	**Particle size**	**Concentration**	**Trap geometry**	**Trap depth**	**Density of traps (pitch)**	**Solution**	**Contact angle or Surface Tension**	**Speed μM.s^{-1}**	**Temperature (°C)**	**Ref**
Polymer resist	Au spheres	50 nm	NA	**Individual** spherical traps and **clusters** from 50 nm to a few μm	60 nm	1 μm to a few μm	Aqueous	10-30°	Evap. only	60	[31]
SiOx	Au spheres	8 nm	NA	**Individual** spherical traps and **clusters** from 10 nm to a few μm	10 nm	1 μm to a few μm	Aqueous	NA	Evap. only	NA	[31]
Hydrophobic Si	Au rods	110x40 nm	2.54 $\cdot 10^{10}$.mL^{-1}	**Individual** traps 120x60 nm	45 nm	500 nm	0.9 mM CTAB	50° (d)	2	∼ 40 (50%hum.)	[33]
PUA	Ag spheres	66 nm	2 wt% (∼10^{13}.mL^{-1})	**Continuous** grids 150 nm width	450 nm	pitch of 3.2 μm	SDS 1 mM, Triton-X45 0.01 wt%	51.5°	30	30 (30%hum.)	[34]
PDMS	Au spheres	60 nm	$2 \cdot 10^{11}$.mL^{-1}	**Individual** traps and **continuous** lines with varied width	40-45 nm for individual and 70-100 nm for lines	1-2 μm	SDS 1 mM, Triton-X45 0.01 wt%	50-60° (d)	NA	27 (50%hum.)	[28]
PDMS	Au rods	80x25 nm	10^{12}.mL^{-1}	**Individual** traps (50 x 140 nm)	37 nm	500 nm	CTAB 0.9 mM	50-55° (static), 35° (d)	0.5-1	50-55	[35]
PDMS	Au rods	70x25 nm	$1.3 \cdot 10^{12}$.mL^{-1}	**Individual** spheric traps (r=60 nm)	40 nm	1 μm	CTAB 0.9 mM	56° (d), 37 mN.m^{-1}	2	∼40	[36]
PDMS	Au spheres	100 nm	$5.6 \cdot 10^{9}$.mL^{-1}	**Individual** spheric traps (r=60 nm)	80 nm	200 nm	commercial nanocube solution	>50° (d)	0.2	28	[26]
PDMS	Au, Ag and Pt spheres	70-80 nm	0.02-0.05 mg.mL^{-1} (∼10^{10}-10^{11}.mL^{-1})	**Individual** particle trapping in small lines	80 nm	1 to 2	SDS 1mM, Triton-X45 0.1 wt%	22 mN.m^{-1}	0.2	40-60	[27]
PDMS	Au rods	64x24 nm	10^{12}.mL^{-1}	**Continuous** assembly in lines (40 nm width)	60 nm	1	CTAB 0.9 mM	50°	0.1	T_{dew} + 28 (∼38 at 50%hum.)	[37]
PMMA on Si/SiO$_2$	nanodiamonds	40 nm	0.001 mg.mL^{-1}	**Individual** spherical traps 45 nm	62 nm	2.6	1% SDS (aqueous)	24°	3.5	24	[32]
PDMS	BaTiO$_3$ spheres	100 nm	1 mg.mL^{-1}	**Individual** particle trapping in dimers 205 x 105 nm	80 nm	NA	SDS 1mM, Triton-X45 0.1 wt%	NA	0.2	T_{dew} + 40 (∼50 at 50%hum.)	[38]
Al (hydrophobic)	Au spheres	110 nm	NA	**Individual** particle trapping in funnel traps 220 nm (neck 20-40 nm)	about 150 nm	0.5	0.3 mM CTAB	40-55°	1.2	45-48	[39]
PDMS	Au prisms	100 nm (7.5 nm thick)	10-50 pM (∼10^{10}.mL^{-1})	**Individual** particle trapping in triangular traps of 150 nm	>20 nm	0.5	0.45 mM CTAB	40-55°	droplet drying (about 4)	40 (40%hum.)	[40]
PDMS	**Au, Ag nanocubes**	**30-40 nm**	**∼10^{12}-10^{13}.mL^{-1}**	**Various aspect ratios (1:1 to 1:10)**	**40 nm**	**250 nm - 5 μm**	**Water-Ethanol or SDS Triton-X45 or 2 mg/ml PVP**	**45-60°**	**1-3 μm/s**	**25-60 (40-70%hum.)**	**This work**

Table 1: State of the art for capillary assembly of sub-100 nm particles. (d)= dynamic contact angle. SDS refers to sodium dodecyl sulfate, and CTAB refers to cetyltrimethylammonium bromide.

2 Results and Discussion

2.1 Guide for capillary assembly of <50 nm nanoparticles

Due to its mechanism, capillary assembly is easier to implement for larger particles. Overall, the method was summarized by Flauraud et al. that identified four important steps: 1) formation of the accumulation zone (AZ), 2) trapping of the particles, 3) resilience upon meniscus receding, 4) drying of the residual solvent in the trap (**Figure 1a**) [33]. Smaller particles being more subject to thermal fluctuations and Brownian motion, it is more difficult for the AZ to build and remain (step 1). In the AZ, particles tend to occupy the entire available volume and thus fill the traps of the template [33, 26, 41]. Nanoparticles, however, have fewer chances to occupy assembly sites because of enhanced diffusivity (step 2) [27, 42].

In the third step, capillary forces come into play to permanently trap nanoparticles in the traps. To this end, the solution in which particles are dispersed is chosen so that in the absence of traps, capillary forces prevent the nanoparticles from depositing, while in the presence of traps, pinning of the meniscus locally changes the direction of the capillary force, pushing particle downwards inside the assembly sites [43]. Continuous pinning and depinning across the template are then responsible for the permanent trapping of particles as the solution recedes [41, 28, 42]. Capillary force, however, decreases with nanoparticles and trap size [31, 27, 40, 33, 28]. Besides, the use of small particles also leads to the use of shallow traps (to facilitate contact printing), degrading the resilience upon meniscus receding. As a result, although capillary assembly was demonstrated to be robust for the assembly of microparticles, the assembly of nanoparticles with a size below 100 nm is still poorly controlled and the working conditions are narrow [27, 42].

Here, we use 40 nm nanocubes (Ag, Au) as probes to investigate the parameter space for capillary assembly of <100 nm nanoparticles. Monodisperse nanocubes are synthesized according to procedures previously reported (see **Figure S1** [44, 45]). After synthesis, nanocubes are redispersed in the solution used for assembly. Requirements for the solution to produce high yield assembly include (i) a static contact angle on PDMS between 40 and 60° (**Figure S2**) and (ii) that nanocubes can be dispersed at a high concentration[26]. We identified two aqueous mixtures, called S1 and S2, composed of 1 mM SDS and 0.01 wt% Triton X-45 and 0.5 mM SDS and 0.005 wt% Triton X-45, enabling to obtain high colloidal stability and contact angles of 45° and 60° respectively, in line with previous reports [28, 34, 27, 46, 41].

Optimal experimental conditions were then found on flat PDMS by monitoring the AZ with the help of an optical microscope mounted on the setup (**Figure S3**). Particle accumulation is induced by a convective flow arising from solvent evaporation and counterbalanced by a recirculation flow in the upper part of the liquid due to the no-slip condition at a fixed wall at the cover slide, bringing nanoparticles back to the bulk of the solution. Thus a higher velocity increases the recirculation flow and depletes the AZ, while a higher temperature, or lower humidity, enhances evaporation and enriches the AZ [26, 28].

At a given speed, there is a temperature threshold beyond which particles accumulate at the front line, as can be appreciated in **Figure 1b** by the orange region arising from gold nanocube structural color (testifying high colloidal concentration), and the crystallized region at the contact line. If the temperature is raised above this point, it increases thermal fluctuations, which is detrimental for particle trapping and can cause AZ precipitation [41]. Using Au nanocubes, we identified conditions for a self-sustained AZ to establish over a flat surface to be 45°C and 55°C for solutions S1 and S2, respectively, at a speed of 1 μm·s^{-1}, humidity of 40%, and particle concentrations of roughly 10^{12} NC·mL^{-1} (**Figures 1b and S4**), which correspond to a surface tension of roughly 25 mN/m in both cases (**Figure S5**).

We then investigated Au and Ag nanocube assembly in molds of different trap sizes designed to accommodate different numbers (1, 2, 3, 5 and 10) of 40 nm nanocubes parallel to the contact line. Traps are organized into staggered arrays. For each trap size there are two sparse arrays (pitch varying from 2 μm to 5 μm) and one dense array (pitch varying between 250 nm to 2 μm) adjacent to each other, as shown in **Figure S6**.

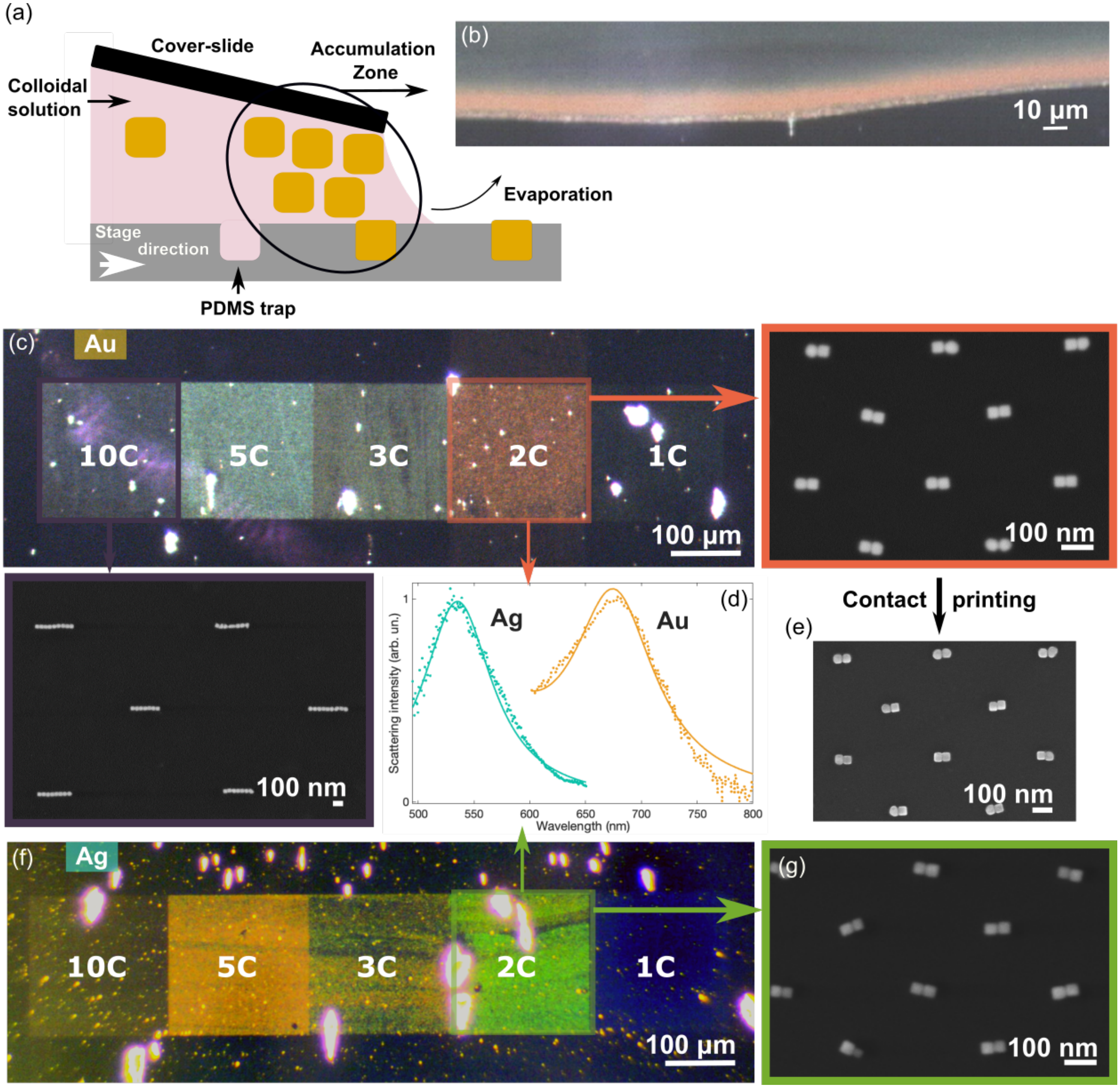

Figure 1: a) Schematic representation of capillary assembly working principle b) Optical image of self-limited and crystalline accumulation zone obtained at 1 μm·s^{-1} and 45°C using gold colloidal solutions c) Optical image showing high yield Au nanocube assembly in the 5 dense arrays and SEM images of dimers (2C) and 10C arrays d) Optical spectra of Ag and Au dimer arrays and the respective Lorentzian fit e) Dimer array deposited from PDMS to silicon by contact printing f) Optical image showing high yield Ag nanocube assembly in the 5 dense arrays g) SEM characterization of the dimer array (Ag).

Assembly experiments were performed with Au nanocubes dispersed in S1 and S2. It confirmed that both solutions could produce nanocube assembly if a dense and self-sustained AZ had been established before entering the assembly zone. A higher assembly yield was obtained with S2 at 0.5 μm·s^{-1}, as shown in **Figure 1c**. Further SEM characterization can be found in SI **Figures S7-S11**, showing good assembly yield at a large area. Figure S12 shows the results for the assembly of 40 nm Au icosahedra, to highlight that the methodology is not limited to nanocubes only.

Figures 1f and g show that arrays of 40 nm Ag nanocubes could be obtained with similar conditions, for traps of various aspect ratios.

However, it is worth noticing that this procedure revealed less reproducible for Ag nanocubes compared to Au nanocubes. This counterintuitive result can only be explained by the different surface chemistry of Ag and Au nanocubes employed in this study, the former being capped with polyvinylpirrolidone (PVP) and the latter with cetyltrimethylammonium chloride (CTAC). We can speculate that due to the larger thickness of the PVP coating compared to CTAC (2-3 nm vs 0.5 nm), van der Waals interactions among nanocubes are weaker for PVP-capped nanocubes. This could result in a AZ in which PVP-capped nanocubes have larger mobility and therefore are more sensitive to external stimuli, compared to CTAC-capped nanocubes that form a highly dense and compact AZ. Mechanistic understanding of the role played by the ligands goes beyond the scope of this work, but our findings that the surface chemistry may play a critical role in the assembly process of nanocubes, are consistent with other reports on nanocube mobility [47, 48].

Array resonances can be tuned by varying trap geometry, nanocube size and material type, corroborating the potential of capillary assembly for the bottom-up fabrication of nanophotonic surfaces. As can be seen in **Figures 1c and f**, different arrays exhibit different scattering resonances which can be appreciated by the different color zones in the optical images (**Figures 1d** shows the scattering spectrum of Au and Ag dimers (2C)). Each colorful array (200×200 μm) highlighted by a contour solid line, corresponds to the area of high trap density. The low-density areas (200×100 μm, situated above and below the dense arrays) show lower assembly yield, despite the identical trap size and assembly conditions, and thus are not clearly visible in the optical images. This unexpected result indicates that macroscopic variables such as contact angle, nanoparticle concentration, speed, etc., are not sufficient to control or fully predict the assembly dynamics, and that other microscopic parameters such as trap density or surface chemistry have a considerable impact on the assembly yield, possibly via a collective action on the pinning-unpinning dynamics of the AZ and its deformation at the scale of the nano-sized traps. Multiphysics simulations of the assembly process, combining hydrodynamics and intermolecular interactions taking place in the entire AZ over one unit cell, would provide enormous insights on the nanoscale dynamics, but are computationally intensive due to the humongous number of nanocubes ($\sim 10^6$) in the AZ. Simplified models have been instead proposed to analyse the forces acting on the particles at the contact line, providing evidence of the impact that some geometrical properties of the template (such as the ratio between the particle size and the trap depth) have on the assembly yield for spherical microparticles [41]. Building on this previous work, we attempt to estimate the impact that pattern density may have on the force balance at the contact line. The meniscus is deformed by the nanocubes in the AZ at the boundary between the solution and air. The deformation acts as an elastic force on the nanocubes and it is responsible for their motion and dragging along the PDMS substrate. The magnitude of this force can be derived from the principle of virtual work (see SI for details):

$$F_{st} = 2\pi\gamma h$$

where γ is the surface tension and h the meniscus deformation assuming a spherical cap. This force is perpendicular to the meniscus surface and, therefore, to the dynamic contact angle. In previous works, this angle has been approximated to the receding contact angle measured on a flat PDMS and in our experimental conditions is $\sim 30°$. The surface tension force F_{st} is in the nN range, going from 0 in the absence of deformation (no AZ present) to ~3 nN for a meniscus deformation on the order of half the particle size. In the AZ, the nanoparticles are closely packed to the extent of forming a crystalline layer. The bottom layer of nanocubes interacts with the PDMS substrate, resulting in a friction force that opposes motion. This has to be balanced by the horizontal component of F_{st}. Note that the entire AZ is moved by the action of surface tension on the nanocubes lying at the solution-water interface. Larger friction requires larger meniscus deformation for AZ motion to take place. This is the case for example when instead of a flat PDMS substrate, the AZ sweeps over a nanopatterned substrate, in which the traps are filled with nanocubes. In this case, even if the trap depth is equal to nanocube size, the van der Waals interaction between the trapped nanocubes and those transiting in close proximity is higher and thus is the friction force. As the pattern density increases, the collective friction force also increases (it scales up by the number of traps in the AZ) and thus it requires a larger meniscus deformation to maintain motion. This is illustrated in Figure 2 for a range of friction coefficients and distances between nanocubes in the

AZ and those in the traps. Hypothesising a nanocube distance of 1.5 nm and a friction coefficient of 0.05, a meniscus deformation of ∼2 nm is obtained for sparse arrays, whereas for dense arrays it is ∼14nm. The factor ∼7 results directly from the ratio of trap density within the AZ. These results indicate that the friction force exerted from trapped nanocubes to those in close proximity in the AZ is not negligible and has to be balanced by a substantial meniscus deformation, which is, as a consequence, function of the pattern density. As a result, the vertical component of F_{st} (opposing nanocubes from escaping the traps due to AZ fluctuations) increases for larger density and can play an important role for the better assembly yield observed.

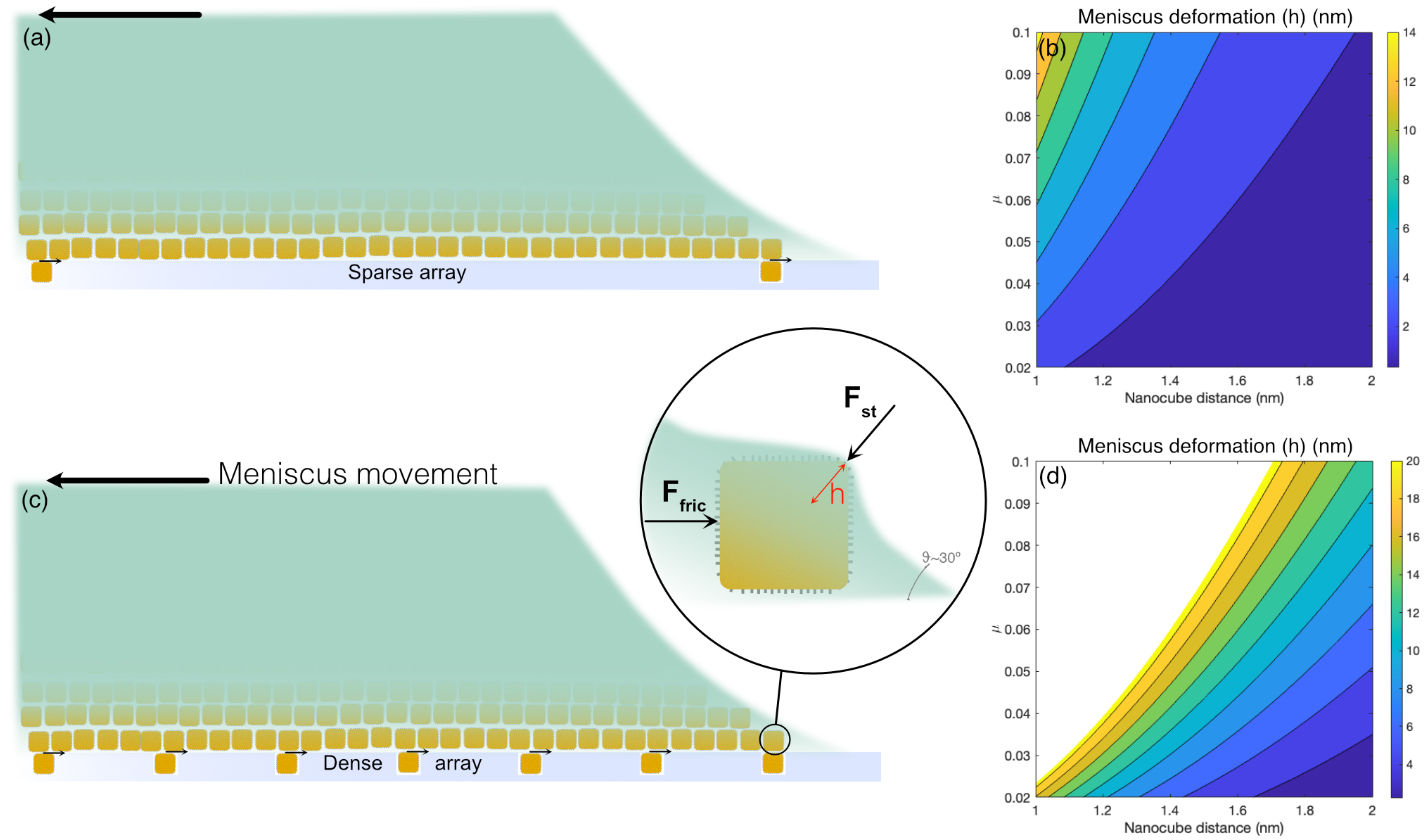

Figure 2: Schematic representation of the AZ for (a) sparse and (c) dense dimer arrays, highlighting the interaction with trapped nanocubes. (b) and (d) represent the meniscus deformation for a range of friction coefficient (μ) and distance between 40 nm nanocubes in the AZ and nanocubes trapped, for sparse and dense arrays, respectively. The meniscus deformation in (d) has been artificially limited to half the nanocube size. The inset in (c) shows the force balance and the meniscus deformation.

Finally, **Figure 1e** shows that such nanocube arrays assembled in 40 nm deep traps could be deposited on arbitrary substrates using contact printing.

This work revealed that due to the narrow working conditions, monitoring AZ properties was of paramount importance to assemble sub-50 nm particles with high yield. Besides, if no assembly could be obtained prior to the formation of a highly crystalline AZ, a too large AZ also resulted in a lower assembly yield. We hypothesize that it arises from strong van der Waals interactions between nanocubes in the AZ in that configuration, preventing them from remaining in PDMS trenches as individual units. Furthermore, we found that when performing the assembly in the presence of a highly crystalline AZ, defects were over-represented in PDMS traps (**Figure S14**), which presumably arises from an entropy-driven exclusion of defects in the AZ (more details in SI). Thus, it supports our hypothesis that van der Waals interactions between nanocubes cannot be neglected. Additionally, the experiments performed with PVP-capped nanocubes (Ag) appear to indicate that steric repulsion due to the type of ligand should also be taken into account in experimental design.

Finally, due to the narrow working conditions and the detrimental impact of large and highly crystalline AZ, large area assembly of sub-50 nm particles would require maintaining the AZ in a steady state by compensating solvent evaporation through continuous solvent inflow, which can be challenging to implement without disturbing solution flow.

2.2 Alternative regime for nanoparticle assembly with a thin AZ

It is thus highly desirable to perform capillary assembly in more stable conditions for which nanocubes interaction can be neglected. The following section aims to give new perspectives and future research areas in that direction.

2.2.1 Aqueous solutions

It is generally admitted that tuning the initial particle concentration (typically from 0.0002 to 0.05 vol% for sub-100 nm particles [49]) can anticipate or delay the appearance of a steady state in the accumulation zone, without affecting assembly yield [27, 50].

We found, however, that in some cases, dilution enables high-yield assembly in a new configuration characterized by the presence of a thin crystalline AZ, as shown in **Figures 3a, b and c** for 40 nm gold nanocubes dispersed at a low concentration in solution S2.

In order to investigate the impact of dilution on the formation of the AZ (and on the assembly quality), concentration was varied while keeping experimental conditions identical. The initial concentration was roughly 10^{12} nanocubes/mL, which allowed us to achieve a dense AZ in a reasonable time (<10 minutes) at 55°C and a speed of 1 μm·s^{-1}. Optical images in **Figure 3d** show the AZs for different dilutions (1, 5, 10 and 20 times) 7 min after the beginning of the experiment. As the solution is more diluted, the contact line displays lighter contrast because of limited accumulation. For a 20-fold diluted solution, however, a threshold is reached, and the contact line again shows starker (but more diffused) contrast. At longer times (10 minutes), a thin crystalline zone formed right at the contact line, followed by a more diffuse AZ higher in the solution (**Figure S15**). Such phenomena, which resulted in high-quality assembly, were found to be reproducible for the 20 times diluted solution but could not be obtained with smaller dilutions, presumably because of different flow dynamics.

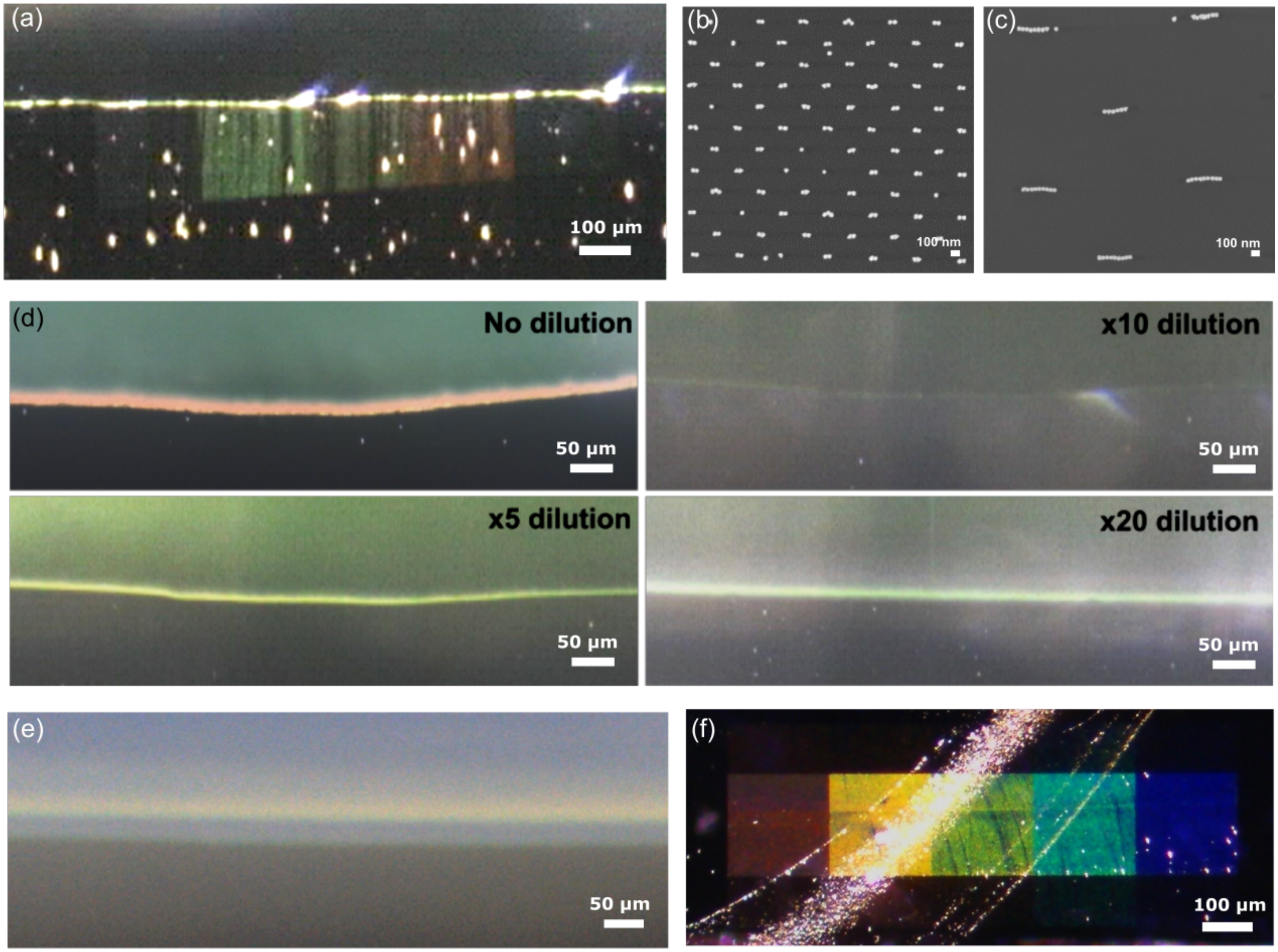

Figure 3: a) Optical image of assembly experiment performed using 10 times diluted 37-nm Au nanocubes in S2 (compared to optimized concentration for high-yield assembly in the presence of a dense accumulation zone of roughly 10^{12} nanocubes/mL) at 50°C, 1 μm·s^{-1}, 40% humidity b, c) SEM images of sample introduced in (a) depicting dimer arrays (b) as well as lines with aspect ratio of 5 (c). d) Optical images taken after 7-min of assembly at 40% humidity, 55°C and 1 μm·s^{-1} upon systematically diluting 39 nm Au nanocubes in S2 e) Optical image of the AZ upon 10 minutes assembly in the presence of 2 mg/mL PVP for a Ag nanocube concentration of roughly $3 \cdot 10^{13}$ NC·mL^{-1} (70% humidity, 60°C and 0.5 μm·s^{-1}) f) Optical image of Ag nanocubes assembled in conditions described in (e) (note that lines cutting through the arrays were deposited after assembly by the remaining solution detaching from the cover slide).

Given the promising results of assembly with a thin and less dense AZ, we attempted to establish a consistent and sustainable methodology that does not rely on the accurate choice of concentration. We hypothesized that by introducing steric repulsions between nanocubes, it would be possible to achieve a AZ that is thin and less dense, regardless of the colloids concentration. PVP appeared to be the ideal candidate to test this hypothesis because, unlike SDS and Triton, it is a polymer and thus can offer conspicuous steric interactions while being at the same time compatible with metal nanoparticles. We introduced PVP in the assembly solution, and found that larger amounts of PVP in the solution led to more diffused accumulation at the contact line **Figure 3e**.

Assembly in such a regime was found to give good and more reproducible results, as shown in **Figure 3f** for 40 nm Ag nanocubes in S2 (1 mM SDS and 0.01 wt% Triton) adjusted with 2 mg/ml of PVP. Note that these results are obtained for a highly concentrated nanocube solution.

It thus appears that solution dilution as well as the introduction of PVP impact the dynamics of nanoparticle motion, inter-particle interactions, and accumulation at the contact line. In this regime, nanocubes can detach more easily from the AZ to occupy PDMS traps, and those trapped are more resilient against AZ fluctuation. This might be particularly relevant for nanocubes, that tend to assemble in close-packed super crystals.

2.2.2 Ligand-free ethanol-water solutions

Finally, we investigated nanocube assembly using ethanol-water solutions. As depicted in **Figure S16**, tuning the ethanol-water ratio enables one to simply tune contact angle and surface tension without introduction of surfactants (see Figure 4). In fact, the opportunity to perform capillary assembly in ligand-free solutions could be interesting to prevent the formation of molecular gaps between the nanopattern and the substrate. In addition, ethanol displays some interesting properties, such as PDMS permeation, high surface tension for moderate contact angles on PDMS, increasing the magnitude of capillary forces, and higher evaporation rate, which enables one to work at higher speed and lower temperature, thus reducing thermal fluctuations.

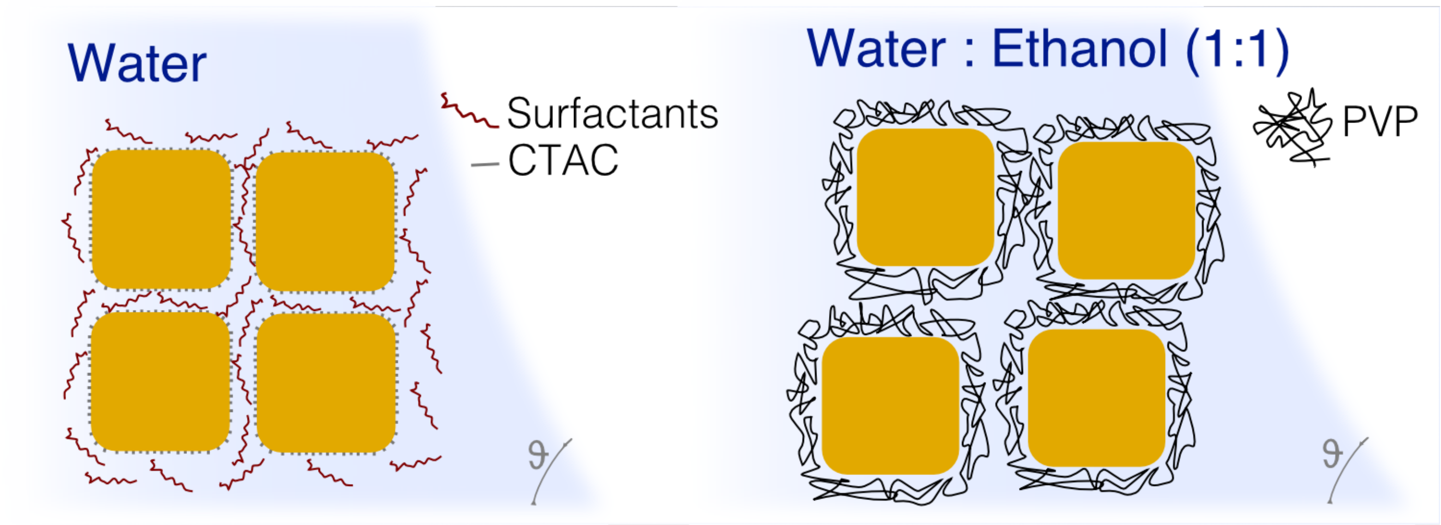

Figure 4: Schematic diagram of water-surfactant (left) and water-ethanol (right) colloidal solutions. Surfactants allow to tune the contact angle and achieve colloidal stability, whereas in surfactant-free solutions, the contact angle is tuned by the water:ethanol ratio, and colloidal stability is achieved via dedicated surface ligands such as PVP.

In order to perform assembly with Au nanocubes, we replaced CTAC ligands (non-soluble in ethanol) with PVP, according to the procedure described in the experimental section. PVP is soluble in polar and non-polar solvents, and adsorbs on the nanocube surface as a 2-4 nm layer, which prevents nanocubes from aggregation. This allows one to achieve high colloidal stability even in the AZ, and it is key to capillary assembly with surfactant-free solutions.

Assembly conditions were investigated by varying ethanol-water ratio from 4-1 to 1-4, nanocube concentration by a factor of 20, temperature between 18 and 25°C and speed between 1 and 4 μm$\cdot$s^{-1}. The formation of a thin crystallized AZ could be observed only at a high temperature or low speed, as shown in **Figure 5a**.

Best assemblies were finally obtained for a 60° contact angle, similarly to solution S2 (Triton and SDS), which corresponds to a 1-1 ethanol-water solution, when performing the assembly around RT in the absence of a crystallized contact line.

Notably, we evidenced preferential assembly in the low-density areas of the arrays when performing the assembly at 3 μm$\cdot$s^{-1}, as depicted in **Figure 5b, c and d**, while assembly in denser areas could be achieved at a lower speed (**Figure 5a**). This is in stark contrast with observations made for Triton and SDS aqueous solutions which always resulted in the preferential assembly of high-density patterns.

It appears to us that the accepted mechanism for capillary assembly is not sufficient to fully explain assembly yield dependence on pattern density, and that interactions taking place inside the AZ and at its boundaries have to be taken into account to provide with a better explanation for our observations. In particular, nanocubes can not be considered as hard spheres that do not interact: strong van der Waals forces among them have to be overcome for insertion in PDMS traps and for resilience, especially when performing assembly in the presence of a dense AZ. Besides, strong interactions between NCs imply that the entire crystallized AZ interacts with the nanopatterns as an ensemble. Reciprocally, it results in a collective action from the traps on the receding meniscus, locally deforming the AZ and affecting the dynamics of NC insertion and resilience, so that trap density can influence the properties of the contact line and the AZ.

Interestingly both Ag and Au nanocubes could be assembled into slightly more complex patterns when performing assembly with water and ethanol solution, such as stair-like patterns shown in **Figure 5e**.

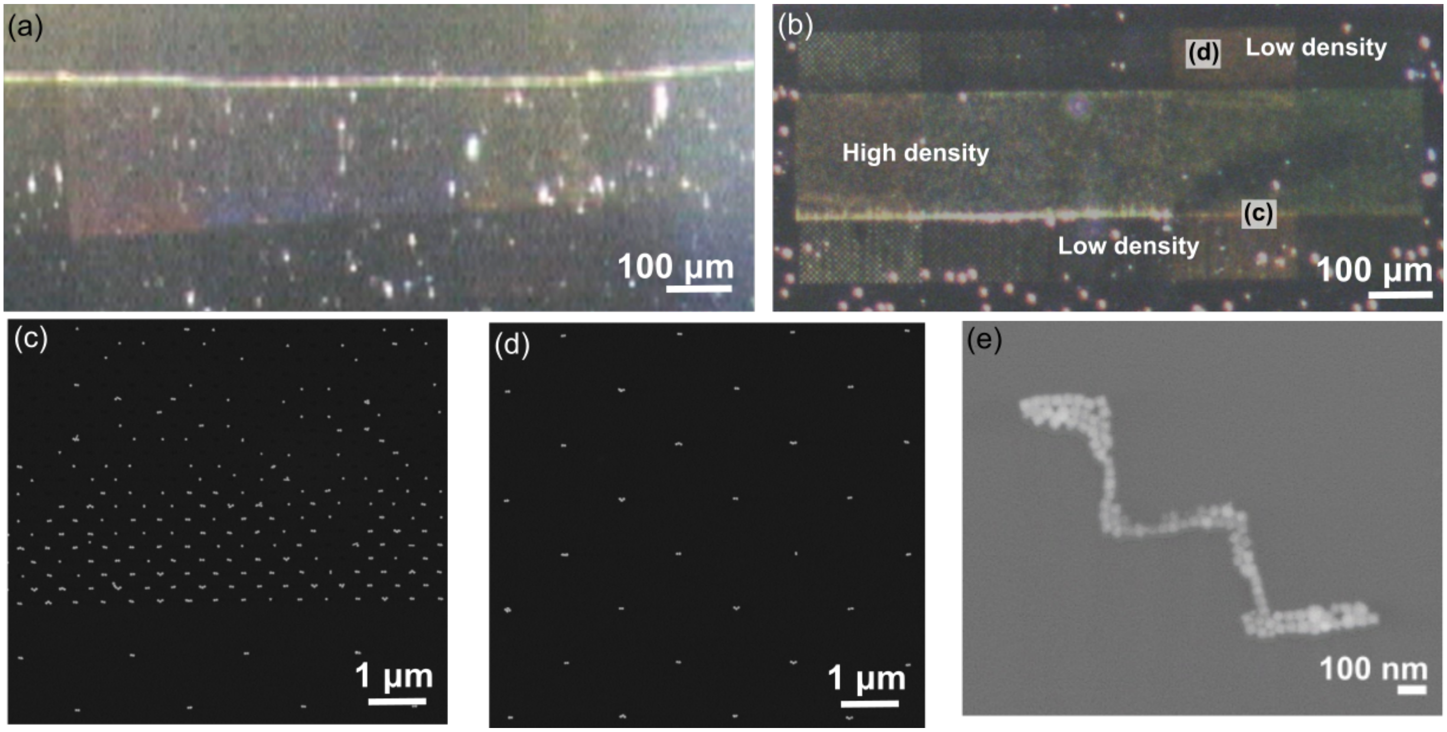

Figure 5: a) Optical image of the contact line showing a very thin accumulation zone when speed is reduced (39 nm Au nanocubes, ethanol-water 1-1 ratio, 25°C 1μm·s^{-1}) b) Preferential assembly of 39 nm Au nanocubes into sparse nanostructure arrays (39 nm Au nanocubes, ethanol-water 1-1 ratio, 25°C 3μm·s^{-1}). SEM images showing 39 nm Au nanocubes assembly in c) dense dimer array, showing that only the first few rows are assembled d) sparse (low density) dimer array e) Fully assembled stair-like nanostructure with 37 nm Ag nanocubes. b-e were assembled at ethanol-water 1-1 ratio, 25°C 3μm·s^{-1}, 60% humidity.

2.3 Nanocube epitaxy for the formation of continuous nanostructures

Finally, we show that nanocubes within the same trap can be welded together at near ambient temperature to obtain continuous plasmonic nanostructure arrays of arbitrary shape, both for Au and Ag. During Au nanocube epitaxy, atoms in solution or in high energy sites (such as corners) migrate to the sub-nanometer gap, forming continuous monocrystalline nanostructures of the highest quality. This is enabled by the 4-fold rotational invariance of single-crystal nanocubes, that ensures identical crystallographic orientation of adjacent units [30]. This new strategy was adapted to produce robust welding for Ag nanocubes in the absence of a reducing agent, which resolved nucleation issues encountered with the overgrowth method reported before for silver [29], and enables to perform nanocube epitaxy directly on the PDMS substrate [51].

The results are summarized in **Figure 6**, showing plasmonic arrays supported on a PDMS substrate with various aspect ratios, both for Ag and Au. These results highlight that the final nanostructure shape is dictated by the nanopattern design, and as a consequence full control over capillary assembly is the key step to achieve large area arrays with individual nanostructure accuracy.

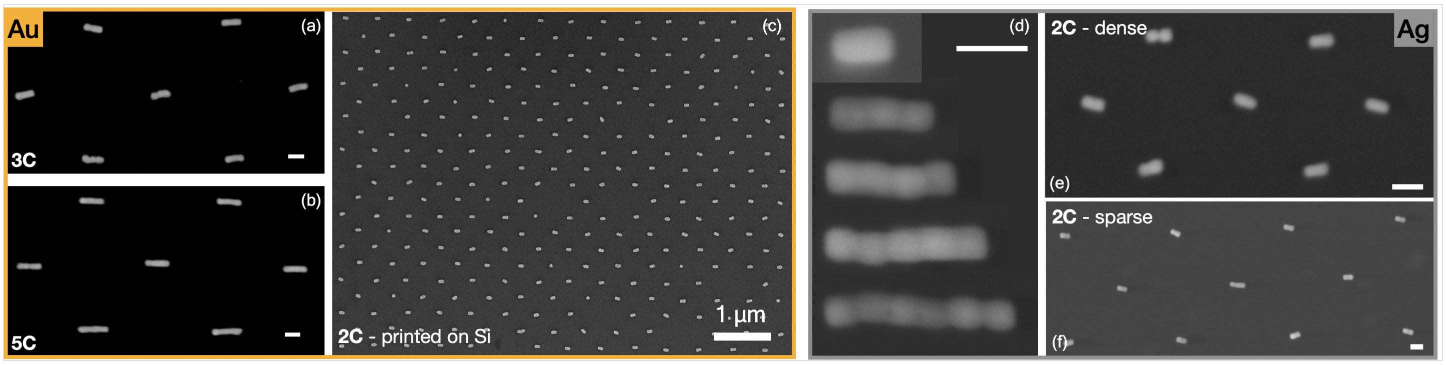

Figure 6: SEM images of assorted plasmonic arrays obtained via capillary assembly followed by nanocube epitaxy for Au (a-c) and Ag (d-f). Adjacent nanocubes are welded into continuous nanostructures, maintaining the spatial organisation secured by capillary assembly. After nanocube epitaxy, the plasmonic arrays can be transferred from PDMS to a new substrate such as silicon via contact printing (c). All scale bars are 100 nm unless stated otherwise.

3 Conclusion

We showed that fine control over the experimental parameters allows for the assembly of multiple sub-50 nm particles in shallow traps, with similar conditions to that previously reported for larger nanoparticles and microparticles.

Monitoring AZ properties to induce a dense accumulation zone preceded by a thin crystalline line using surfactant-stabilized aqueous solutions enabled us to identify optimal conditions for the assembly of 40 nm nanocubes into simple patterns. This enabled the realization of 1D nanostructure arrays with control over the geometry comparable to EBL, but with high potential for scalability, low cost and high material quality. These arrays can be engineered to display a specific optical response simply by optimising the EBL master design, integrated on a device via contact printing, and finally constitute an ideal platform to develop and study nanocube epitaxy.

The narrow range of experimental parameters in which nanoparticles can be assembled, makes the technique highly sensitive to perturbations, in addition to the lack of neat understanding of some of the parameters' impact. Assembly quality appears to strongly depends on AZ properties, which not only is influenced by the assembly solution (particle geometry, capping ligands, concentration, solution contact angle and surface tension, etc.) and assembly parameters (temperature, speed, humidity), but also by the pattern density, that has an impact on the meniscus deformation. Achieving reproducible assembly at a high yield is extremely challenging, as these critical parameters often vary with time, are interdependent and may not be entirely controllable.

Solution dilution, the introduction of surfactants and the use of ethanol-water solutions, allowed to perform assembly in a more stable regime. Ethanol-water solutions, in particular, gave interesting perspectives for the assembly of arbitrary shape patterns as well as sparse patterns. However, more systematic studies are needed to achieve a deeper understanding of their working mechanisms and to account for pattern density effects.

Finally, we showed that nanocubes could be epitaxially connected to form monocrystalline nanostructure arrays in a PDMS mold, showing that the combination of templated assembly and nanocube epitaxy is highly promising for the realization of flexible and printable surfaces for optoelectronics and nanophotonics.

4 Experimental Section

Materials: PDMS was purchased from ABCR Germany, $HAuCl_4$, HNO_3, NaBr, CF_3COOAg, CTAC (25 wt% in H_2O), CTAB, NaSH, HCl, Ethylene Glycol, PVP (55,000 Mw), Triton X-45, SDS, ascorbic acid, absolute ethanol and $NaBH_4$ were purchased from Merck at the highest purity available. Deionized water (18.2 MΩ·cm) was taken from a Milli-Q Direct 8 system (Merck).

Nanocube synthesis:
40 nm **Ag nanocubes** were synthesized following a procedure from Xia's group [52]. Briefly, 25 mL of ethylene glycol was pre-heated in a round-bottom flask using a 155°C oil bath at a stirring speed of 200 rpm. 300 μL of 3 mM NaSH was then added to the solution. After 2 min, 2.5 mL of HCl 3 mM and 6.25 mL of 20 mg/mL PVP were quickly added. After another 2 min, 2 mL CF_3COOAg 282 mM was added to the round bottom flask. The reaction was finally quenched using an ice-cold water bath after 1H30.
Nanocubes were washed twice by centrifugation and redispersed in ultrapure water at a concentration of roughly $2{\cdot}10^{14}$ nanocubes/mL (Figure S1).

40 nm **Au nanocubes** were synthesized following Park *et al.* procedure [45]. Briefly, 10 nm CTAC-capped seeds were overgrown in a 50 mL round bottom flask using 6 mL of 100 mM CTAC, 30 μL of 40 mM sodium bromide, 100 μL of the 10 nm seed solution at 2 OD in 20 mM CTAC, 390 μL of 10 mM ascorbic acid and 6 mL of 0.5 mM $HAuCl_4$ solution. The solution was left to react for 25 minutes at RT with gentle stirring prior to centrifugation. The nanocube solution was washed twice and redispersed in 10 mL of ultrapure water at a concentration of roughly $2{\cdot}10^{12}$ nanocubes/mL (Figure S1).

40 nm **Au icosahedra** were synthesized using a procedure modified from nanocubes synthesis reported by Park et al. [45]. 6 mL of 100 mM CTAC, 58 µL of 10 nm seed solution, 390 µL of 10mM ascorbic acid, and 6 mL of 0.5 mM HAuCl4 solution were added consecutively into a 50 mL round-bottomed flask. While doing so, the solution was stirred at 500 rpm, after which the stirring was reduced to 200 rpm for 25 minutes at RT. Finally, the solution was washed twice and redispersed in 10 mL of ultrapure water at a concentration of roughly $1.4{\cdot}10^{10}$ (Figure S12).

Ligands could then be exchanged from CTAC to PVP for specific needs using Fan et al. procedure (modified) [53]. Roughly 100 μL of 50 mg/mL PVP (Mw 55000 $g.mol^{-1}$) in water and 3 mL ethanol were added to 1 mL of 1 OD (10^{12} nanocubes/mL) CTAC capped Au nanocubes stock solution. The solution was stirred for about 48H at RT before centrifuging nanocubes twice (9000 rpm, 10 minutes) to remove excess PVP completely. Nanocubes could then be re-dispersed in ethanol.

Molds fabrication:
Silicon master were realized by e-beam lithography using PMMA resist on silicon. Upon exposition and development, a thin layer of chrome was evaporated on the substrate to be used as a hardmask. PMMA was then lifted-off in acetone. Silicon was then etched by 40 nm using Reactive Ion Etching (RIE). Chrome was finally removed using a commercial chrome etchant.

Masters were then silanized with 1H,1H,2H,2H-Perfluorooctyltriethoxysilane in a desiccator upon plasma treatment to ease PDMS demolding.

Silicon masters were replicated to PDMS on a glass slide. PDMS was prepared by mixing 1 quantity (by mass) of prepolymer Vinylmethysiloxane (AB 116647), 5 ppm of Pt catalyst (platinumdivinyltetramethyldisiloxane complex in xylene), 0.1 wt% of modulator (2,4,6,8-tetramethyltetravinyl cyclotetrasiloxane) and 1.25 quantity of the second prepolymer (hydrosilane, AB 109380), all purchased from ABCR Germany. The first three components were mixed prior to adding the second prepolymer. PDMS was then cured at 150°C for 20 minutes on a hotplate. The PDMS molds were then stored in ethanol for at least a few days prior to assembly to remove un-reacted species in PDMS.
For contact printing experiment, commercial PDMS from Wacker (RT601) mixed in a 9-1 ratio and cured at 100°C for 10 minutes on a hotplate was preferred.

Capillary assembly: Capillary assembly was performed on a homemade setup composed of a moving stage (x direction), equipped with a Peltier element on which was deposited the PDMS substrate, a glass slide substrate holder moving in the z direction, and an optical microscope enabling to monitor capillary assembly *Operando*. All elements were purchased from Thorlabs and controlled by a homemade labview software (Figure S3).

The nanocube solutions were centrifuged at 9,000 RPM for 10 minutes and redispersed in assembly solutions. A hydrophobic glass slide (treated with perfluorodecyltrichlorosilane in the presence of acetic acid in a desiccator) was placed above the nanostructured PDMS template and the colloidal nanocube solution was introduced between the PDMS and the glass slide with a micropipette (roughly 60 μL). Assembly was performed by dragging the nanocube solution over the PDMS substrate by displacing the moving stage at a controlled speed (0.2-5 μm.s^{-1}). Evaporation was controlled by monitoring temperature and humidity, which could be varied by flowing nitrogen with different degrees of humidity into a close chamber mounted around the capillary assembly setup, as depicted in Figure S3. Typical experiments were performed under 40% humidity.

Silver nanocube epitaxy on flat PDMS: Typically, 2 μL of an aqueous nanocube solution were dropcasted on flat PDMS substrates. Ligands were always removed after complete evaporation of the solution by dipping the PDMS substrate sequentially in ultrapure water, acetone, isopropanol and ultrapure water again (one minute each) to have the substrate as clean as possible before ligand desorption. The ligands adsorbed on the nanocube surface were then removed by exposing the substrate to a 100 mM $NaBH_4$ solution for 30 minutes. Hydrides having a higher binding affinity to gold effectively displace the ligands, as reported in ref. [54]. Finally, samples were rinsed thoroughly with ultrapure water.

Weldings were performed by introducing the substrates into 20 mL vials containing 10 mL of welding solutions using a water bath, with no agitation. The standard welding procedure on flat PDMS was 60°C for 1 hour in the presence of 25 μM NaBr and 100 μL of HNO_3.

Silver nanocube epitaxy upon capillary assembly: Assemblies are left to fully dry in air for at least an hour before removing the ligands with the strategy described above (when dipping the samples in $NaBH_4$ right after assembly, part of the assembly would come off the substrate). Welding was performed by introducing the PDMS substrate into a solution containing CF_3COOAg 10 mM and 100 μL of HNO_3 (for a total volume of 10 mL). Reactions were performed at 60°C for one hour, with no agitation. Upon welding, substrates were rinsed with ultrapure water and dried with a stream of nitrogen.

Printing: Printing was performed on silicon substrates. Oxygen plasma (10 minutes, 200W, 150°C) was first performed, then 1μL of PMMA was deposited was dropcasted on the substrate to act as an adhesion layer at 20°C and the PDMS sample was slowly put in contact and pressed on the silicon substrate before evaporation of the solvent. The whole process was monitored using optical microscope by looking through the transparent PDMS, to ensure good contact between the two substrates and to position assembled areas on silicon. When the two substrates were entirely in contact, the temperature was then raised and maintained at 50°C for 10 minutes for the solvent to dry. Upon releasing the pressure nanocubes remained on the silicon towards which they have higher affinity.

Characterization: Assemblies of nanocubes on PDMS were imaged using a scanning electron microscope (JEOL 7900F) in low vacuum mode with a pressure of 60 Pa.
TEM and electron diffraction was performed with a JEOL 2100F. Optical characterisation was performed with an inverted microscope (Zeiss Axiovert 200M) with an air objective (100X, NA = 0.9) in reflection. The PDMS without nanoantennas was used as the reference to take into account of the spectral response of the system. Light was coupled into a 25 μm optical fiber, yielding a collection spot diameter of ∼1.3 μm.

Supporting Information

Supporting Information is available from the Wiley Online Library or from the author.

Acknowledgements

The authors thank Oznur Gulabigul for gold nanocube synthesis, Peeranuch Poungsripong for silver nanocube synthesis and F. Bedu for support with e-beam lithography. B. Sciacca thanks AMUtech, MITI

CNRS (project COMPACT) and ANR (project MeMeNtO) for funding.

References

[1] H. J. Lee, S. Oh, K. Y. Cho, W. L. Jeong, D. S. Lee, S. J. Park, ACS Applied Materials and Interfaces **2018**, 10, 16 14124.

[2] S. a. Maier, Fundamentals and Applications Plasmonics : Fundamentals and Applications, **2007**.

[3] M. S. Bin-Alam, O. Reshef, Y. Mamchur, M. Z. Alam, G. Carlow, J. Upham, B. T. Sullivan, J. M. Ménard, M. J. Huttunen, R. W. Boyd, K. Dolgaleva, Nature Communications **2021**, 12, 1 974.

[4] K. L. Kelly, E. Coronado, L. L. Zhao, G. C. Shatz, Journal of Physical Chemistry B **2003**, 107 668.

[5] R. Keunen, D. MacOretta, N. Cathcart, V. Kitaev, Nanoscale **2016**, 8, 5 2575.

[6] S. Eustis, M. A. El-Sayed, Chemical Society Reviews **2006**, 35, 3 209.

[7] G. Baffou, R. Quidant, Chemical Society Reviews **2014**, 43, 11 3898.

[8] H. A. Atwater, A. Polman, Nature Materials **2010**, 9, 3 205.

[9] Q. Shi, T. U. Connell, Q. Xiao, A. S. Chesman, W. Cheng, A. Roberts, T. J. Davis, D. E. Gómez, ACS Photonics **2019**, 6, 2 314.

[10] S. Nie, S. R. Emory, Science **1997**, 275, 5303 1102.

[11] K. A. Willets, R. P. Van Duyne, Annual Review of Physical Chemistry **2007**, 58 267.

[12] J. Nuñez, A. Boersma, J. Grand, S. Mintova, B. Sciacca, Advanced Functional Materials **2021**, 31, 24 2101623.

[13] E. Cortés, W. Xie, J. Cambiasso, A. S. Jermyn, R. Sundararaman, P. Narang, S. Schlücker, S. A. Maier, Nature Communications **2017**, 8 14880.

[14] M. Navlani-García, D. Salinas-Torres, K. Mori, Y. Kuwahara, H. Yamashita, Catalysis Surveys from Asia **2019**, 23, 3 127.

[15] S. Linic, U. Aslam, C. Boerigter, M. Morabito, Nature Materials **2015**, 14, 6 567.

[16] J. N. Anker, W. P. Hall, O. Lyandres, N. C. Shah, J. Zhao, R. P. V. Duyne, Nature Materials **2008**, 7 442–.

[17] X. Yang, M. Yang, B. Pang, M. Vara, Y. Xia, Chemical Reviews **2015**, 115, 19 10410.

[18] F. Yesilkoy, R. A. Terborg, J. Pello, A. A. Belushkin, Y. Jahani, V. Pruneri, H. Altug, Light: Science & Applications **2018**, 7, 2 17152.

[19] A. Shakoor, B. C. Cheah, D. Hao, M. Al-Rawhani, B. Nagy, J. Grant, C. Dale, N. Keegan, C. McNeil, D. R. S. Cumming, ACS Photonics **2016**, 3, 10 1926.

[20] A. Biswas, I. S. Bayer, A. S. Biris, T. Wang, E. Dervishi, F. Faupel, Advances in Colloid and Interface Science **2012**, 170, 1-2 2.

[21] L. Sun, C. Zhang, C. Y. Wang, P. H. Su, M. Zhang, S. Gwo, C. K. Shih, X. Li, Y. Wu, Scientific Reports **2017**, 7, 1 3.

[22] S. H. Chew, A. Gliserin, S. Choi, X. T. Geng, S. Kim, W. Hwang, K. Baek, N. D. Anh, Y. J. Kim, Y. M. Song, D. E. Kim, S. Y. Jeong, S. Kim, Applied Surface Science **2020**, 521 146377.

[23] Y. Wu, C. Zhang, N. M. Estakhri, Y. Zhao, J. Kim, M. Zhang, X. X. Liu, G. K. Pribil, A. Alù, C. K. Shih, X. Li, Advanced Materials **2014**, 26, 35 6106.

[24] H. Zhang, C. Kinnear, P. Mulvaney, Advanced Materials **2020**, 32, 18 1.

[25] N. J. Halas, S. Lal, W.-S. Chang, S. Link, P. Nordlander, Chemical Reviews **2011**, 111, 6 3913.

[26] L. Malaquin, T. Kraus, H. Schmid, E. Delamarche, H. Wolf, Langmuir **2007**, 23, 23 11513.

[27] S. Ni, H. Wolf, L. Isa, Langmuir **2018**, 34, 7 2481.

[28] T. Kraus, L. Malaquin, H. Schmid, W. Riess, N. D. Spencer, H. Wolf, Nature Nanotechnology **2007**, 2, 9 570.

[29] B. Sciacca, A. Berkhout, B. Brenny, S. Oener, M. van Huis, A. Polman, E. Garnett, Advanced Materials **2017**, 29, 26 1701064.

[30] A. Capitaine, B. Sciacca, Advanced Materials **2022**, 34, 24 2200364.

[31] Y. Cui, M. T. Björk, J. A. Liddle, C. Sönnichsen, B. Boussert, A. P. Alivisatos, Nano Letters **2004**, 4, 6 1093.

[32] H. J. Shulevitz, T. Y. Huang, J. Xu, S. J. Neuhaus, R. N. Patel, Y. C. Choi, L. C. Bassett, C. R. Kagan, ACS Nano **2022**, 16, 2 1847.

[33] V. Flauraud, M. Mastrangeli, G. Bernasconi, J. Butet, D. Alexander, E. Shahrabi, O. Martin, J. Brugger, Nature Nanotechnology **2017**, 12, 1 73.

[34] J. Kang, C. G. Park, S. H. Lee, C. Cho, D. G. Choi, J. Y. Lee, Nanoscale **2016**, 8, 21 11217.

[35] C. Kuemin, L. Nowack, L. Bozano, N. D. Spencer, H. Wolf, Advanced Functional Materials **2012**, 22, 4 702.

[36] C. Kuemin, R. Stutz, N. D. Spencer, H. Wolf, Langmuir **2011**, 27, 10 6305.

[37] A. Rey, G. Billardon, E. Lörtscher, K. Moth-Poulsen, N. Stuhr-Hansen, H. Wolf, T. Bjørnholm, A. Stemmer, H. Riel, Nanoscale **2013**, 5, 18 8680.

[38] F. Timpu, N. R. Hendricks, M. Petrov, S. Ni, C. Renaut, H. Wolf, L. Isa, Y. Kivshar, R. Grange, Nano Letters **2017**, 17, 9 5381.

[39] H. S. Yu, A. Conde-Rubio, H. C. Wang, O. J. Martin, G. Boero, J. Brugger, Particle and Particle Systems Characterization **2022**, 39 2100288.

[40] Y. Zhou, X. Zhou, D. J. Park, K. Torabi, K. A. Brown, M. R. Jones, C. Zhang, G. C. Schatz, C. A. Mirkin, Nano Letters **2014**, 14, 4 2157.

[41] S. Ni, J. Leemann, H. Wolf, L. Isa, Faraday Discuss. **2015**, 181 225.

[42] S. Mehraeen, M. Asbahi, W. Fuke, J. Yang, J. Cao, M. C. Tan, Langmuir **2015**, 31, 31 8548.

[43] C. Shillingford, V. Grebe, A. McMullen, J. Brujic, M. Weck, Langmuir **2019**, 35, 37 12205.

[44] Q. Zhang, W. Li, L.-P. Wen, J. Chen, Y. Xia, Chemistry-A European Journal **2010**, 16, 33 10234.

[45] J. E. Park, Y. Lee, J. M. Nam, Nano Letters **2018**, 18, 10 6475.

[46] S. Ni, J. Leemann, I. Buttinoni, L. Isa, H. Wolf, Science Advances **2016**, 2, 4 e1501779.

[47] H. Agrawal, E. C. Garnett, ACS Nano **2020**, 14, 9 11009.

[48] A. Capitaine, M. Bochet-Modaresialam, P. Poungsripong, C. Badie, V. Heresanu, O. Margeat, L. Santinacci, D. Grosso, E. Garnett, B. Sciacca, ACS Nano **2023**.

[49] S. Ni, L. Isa, H. Wolf, Soft Matter **2018**, 14, 16 2978.

[50] F.-D. Delapierre, G. Mottet, V. Taniga, J. Boisselier, J.-L. Viovy, L. Malaquin, Biofabrication **2017**, 9, 1 15015.

[51] L. M. Fajri, A. Capitaine, B. Sciacca, Manuscript in preparation **2023**.

[52] Q. Zhang, W. Li, C. Moran, J. Zeng, J. Chen, L. P. Wen, Y. Xia, Journal of the American Chemical Society **2010**, 132, 32 11372.

[53] Q. Fan, H. Yang, J. Ge, S. Zhang, Z. Liu, B. Lei, T. Cheng, Y. Li, Y. Yin, C. Gao, Research **2020**, 2020 2131806.

[54] S. M. Ansar, F. S. Ameer, W. Hu, S. Zou, C. U. Pittman, D. Zhang, Nano Letters **2013**, 13, 3 1226.

[55] G. Van Anders, D. Klotsa, N. K. Ahmed, M. Engel, S. C. Glotzer, Proceedings of the National Academy of Sciences of the United States of America **2014**, 111, 45 4812.

[56] B. C. Rocha, S. Paul, H. Vashisth, Entropy **2020**, 22, 8.

[57] M. E. King, I. A. Kent, M. L. Personick, Nanoscale **2019**, 11 15612.

[58] P. L. Redmond, A. J. Hallock, L. E. Brus, Nano Letters **2005**, 5, 1 131.